(3 + 1)-dimensional Schwinger pair production with quantum computers

Bin Xu[*] and Wei Xue[†]

Department of Physics, University of Florida, Gainesville, Florida 32611, USA

Real-time quantum simulation of quantum field theory in $(3 + 1)$D requires large quantum computing resources. With a few-qubit quantum computer, we develop a novel algorithm and experimentally study the Schwinger effect, the electron-positron pair production in a strong electric field, in $(3 + 1)$D. The resource reduction is achieved by treating the electric field as a background field, working in Fourier space transverse to the electric field direction, and considering parity symmetry, such that we successfully map the three spatial dimension problems into one spatial dimension problems. We observe that the rate of pair production of electrons and positrons is consistent with the theoretical predication of the Schwinger effect. Our work paves the way towards exploring quantum simulation of quantum field theory beyond one spatial dimension.

I. INTRODUCTION

Historically, the development of quantum electrodynamics (QED) significantly advances the understanding of quantum field theory (QFT) in its early stage. Quantum simulation of QFT [1–5] has a great potential to revolutionize fundamental physics, in part because it can simulate highly entangled quantum systems. The quantum simulation may solve the problems that are hard to achieve by analytical calculations, e.g., high-energy hydrogen collision, a nonperturbative preheating process in the early universe [6–8], and many-body problem for collective neutrino oscillations [9–11]; and it may help us understand the dynamics of quantum systems, since the Monte Carlo simulations using lattice-field-theory techniques in classical computers are limited by the sign problem [12,13]. Currently, it is in its very early stage and QED can play a similar role to make progress in simulating QFT in quantum computers.

The Schwinger mechanism [14], as a textbook example in QED, is employed to improve our knowledge of quantum algorithms for QFT. The mechanism describes electron-positron pair production from a strong electric field **E**. The pair production is viewed as a nonperturbative phenomenon of vacuum decay. Also, it can be understood from a QED effective action by considering quantum corrections from the interactions of the electric field and virtual electron-positron pairs. It has been invoked to gain insights on particle production in QCD [15–19] and on black hole physics [20,21]. To produce the electron-positron pair in the laboratory, the electric field needs to reach the critical value $E_{\text{critical}} \sim 10^{18}$ volts/meter, which is extremely strong and not accessible by current experiments. All these motivate us to study the Schwinger effect with quantum computers.

We are in the noisy intermediate-scale quantum (NISQ) era [22], in which the quantum computing power is limited by its size and the imperfect control of noises. Even with the imperfect quantum hardware, some progress of QFT simulation has been made in both developing quantum algorithms [23–40] and performing quantum simulation [41–54]. However, limited by the small-scale quantum computers, most of the simulations for QFT are demonstrated in $(1 + 1)$D. In particular, the previous realization of the Schwinger effect on quantum computers is only done in $(1 + 1)$D [47,48]. Going beyond one spatial dimension is a crucial step towards exploring more fundamental questions in QFT. In this article, we present a novel method to simulate the Schwinger effect in $(3 + 1)$D only with a few qubits. This method can apply to other field theory questions beyond one spatial dimension.

Because of the significance of the Schwinger mechanism, it is worthwhile to run a real-time simulation and compare the results to the theoretical predication. To simulate the Schwinger pair production, we discretize the space along the direction of the electric field and scan the momentum space along the direction perpendicular to the electric field. Inspired by [48], we impose the parity symmetry to further reduce the number of qubits by half, and eventually the algorithm is implemented on an IBM digital quantum computer with 5 qubits. The particle-antiparticle pair production is observed in the real-time simulation as expected, and the production rate agrees with the predication of the Schwinger effect within uncertainties.

[*]binxu@ufl.edu
[†]weixue@ufl.edu

The article is structured as follows. In Sec. II we introduce the theoretical setup for quantum simulation of the Schwinger mechanism. A detailed description of the algorithm is presented in Sec. III. We show the main results of our algorithm and analyze the errors in Sec. IV. Finally, we conclude and discuss our anticipation for future works in Sec. V.

II. THEORETICAL SETUP

In the NISQ era, quantum simulation is limited to a few qubits and has large quantum noises, which challenges the quantum simulation of QFT in $(3+1)$D. To experimentally study the Schwinger pair production in $(3+1)$D, we introduce several techniques to simplify and parallelize the quantum simulation, including the background field method, dimension reduction, parity symmetry, etc.

We treat the gauge field A^μ as a classical background field since we are not concerned with the dynamics of A^μ. A fermion field ψ interacting with the gauge field A^μ is described by the following action,

$$S = \int d^4x [\bar{\psi}(i\not{D} - m)\psi], \quad (1)$$

where $\not{D} = (\partial_\mu + ieA_\mu)\gamma^\mu$. Here we choose the axial gauge with $A_z = 0$ and $A_0 = -E|z|$ to give a static electric field $\mathbf{E}$ in the z direction. The background field approach is in accord with the principle of the Euler-Heisenberg Lagrangian derived from the effective action to predict the Schwinger pair creation rate, where A_μ is a background field and fermions are integrated out. This approach also implies that we neglect the backreaction of the produced electrons and positrons to the electric field and interactions among the electrons and positrons.

We observe that the Hamiltonian can be diagonalized by a unitary transformation. Thus a $(3+1)$D simulation is decomposed into a summation of several $(1+1)$D simulations, which dramatically reduce the number of qubits in the quantum simulation. The reduction is realized by working in the Fourier space of (x, y) and the real space of z. The Fourier decomposition of fermions takes the form

$$\psi(\mathbf{x}) = \int \frac{dp_x dp_y}{(2\pi)^2} \sum_s \psi_s(p_x, p_y, z) e^{i(p_x x + p_y y)}, \quad (2)$$

with summation over the spin s. By taking a unitary transformation,

$$U = \begin{pmatrix} \sqrt{m'+m} & -\frac{p_x\sigma_x + p_y\sigma_y}{\sqrt{m'+m}} \\ \frac{p_x\sigma_x + p_y\sigma_y}{\sqrt{m'+m}} & \sqrt{m'+m} \end{pmatrix} \quad (3)$$

with $m' \equiv \sqrt{m^2 + p_\perp^2}$ and $p_\perp \equiv \sqrt{p_x^2 + p_y^2}$, the fermion field is rotated as $\tilde{\psi}_s(p_x, p_y, z) = U^\dagger \psi_s(p_x, p_y, z)$, and the Hamiltonian is converted into a 2D form,

$$H = \int dz \frac{dp_x dp_y}{(2\pi)^2} \sum_s \tilde{\psi}_s^\dagger(\pm i\partial_z \tilde{\gamma}^0 \tilde{\gamma}^1 + m'\tilde{\gamma}^0 + eA_0)$$
$$\otimes I_{2\times 2}\tilde{\psi}_s, \quad (4)$$

where $\pm$ correspond to spin-up and -down, respectively. The reduction is achieved by transforming the 4×4 matrix in the Hamiltonian into a 2×2 $\tilde{\gamma}$ matrix times the identity matrix $I_{2\times 2}$. $\tilde{\gamma}^i$ happen to have the same form of gamma matrices in 2D. For a detailed derivation, see Appendix A from Eq. (A3) to (A15). In the new Hamiltonian, m' is an effective mass in $(1+1)$D. Therefore, the Schwinger pair production rate in $(3+1)$D is given by integrating the rate in $(1+1)$D over the transverse momentum and summing over the spin,

$$\Gamma_{3+1}(m) = 2 \int \frac{d^2 p_\perp}{(2\pi)^2} \Gamma_{1+1}\left(m' = \sqrt{m^2 + p_\perp^2}\right). \quad (5)$$

After reducing to two dimensions, we spatially discretize the Hamiltonian with the Kogut-Susskind formulation [55–57], mapping electrons (positrons) into even (odd) lattice sites [see Eq. (A19) in Appendix A]. With the lattice spacing a, the discretized free Hamiltonian H_0 and interaction H_I describing the dynamics of one component of fermion field $\phi(n)$ with periodic boundary condition,

$$H_0 = H_{0,m} + H_{0,k} = m\sum_n (-1)^n \phi^\dagger(n)\phi(n)$$
$$+ \frac{i}{2a}\sum_n [\phi^\dagger(n)\phi(n+1) - \phi^\dagger(n+1)\phi(n)], \quad (6)$$

$$H_I = \sum_n eA_0(na)\phi^\dagger(n)\phi(n), \quad (7)$$

where $H_{0,m}$ is the mass term and $H_{0,k}$ is the kinetic term with nearest-neighbor lattice-site interactions.

Furthermore, by considering the parity symmetry of QED, the Hamiltonian is decomposed into the parity even and odd one. And the parity even/odd fermion fields are $\psi_\pm = (\psi(x) \pm \gamma^0\psi(-x))/\sqrt{2}$ for the continuum case and the staggered lattice fields $\phi_\pm$ are given in the Appendix. The number of spatial sites is reduced by half and the parity even and odd fermions are simulated separately. Eventually these parity even or odd fermions are mapped into Pauli spin operators by using the Jordan-Wigner transformation [58].

III. QUANTUM COMPUTING ALGORITHM

As shown in the previous section that the $(3 + 1)$D Schwinger pair production problem is simplified to 1D lattice, we proceed to simulate this nonperturbative process in digital quantum computers. We start from 10 lattice sites $(0, 9)$, where electron (positron) states are at the even (odd) lattice sites. Then reduce the lattice to $(0, 4)$ by considering parity symmetry. The parity symmetry and ground states are shown in Fig. 1. The gauge field $A_0 = naE$ with n as the lattice number $(0, 4)$. Under the parity transformation, $A_0 = (10 - n)aE$ in the lattice of $(5, 9)$.

The simulation consists of the following main steps: the ground state preparation, time evolution of the parity even Hamiltonian $e^{-iH_+ t}$, and measurement with the interaction turned off, which is illustrated by the schematic quantum circuit,

$$|10101\rangle \;/\!\!\!\!\!\!\!-\!\boxed{U_{VQE}}\!-\!\boxed{e^{-iH_+ t}}\!-\!\boxed{U_{VQE}^\dagger}\!-\!\measuredangle$$
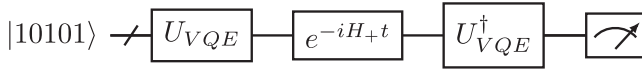
Before and after the time evolution, adiabatic turn-on and turn-off of interactions are essential steps, which are substituted by VQE transformations, U_{VQE} and $U_{\text{VQE}}^\dagger$.

A. Ground state

The ground state of the Hamiltonian with only mass term $H_{0,m} = \sum_{n=0}^{4}(-1)^n m\phi^\dagger(n)\phi(n)$ denoted as $|10101\rangle$ has no electron and positron, which is set as the initial state of
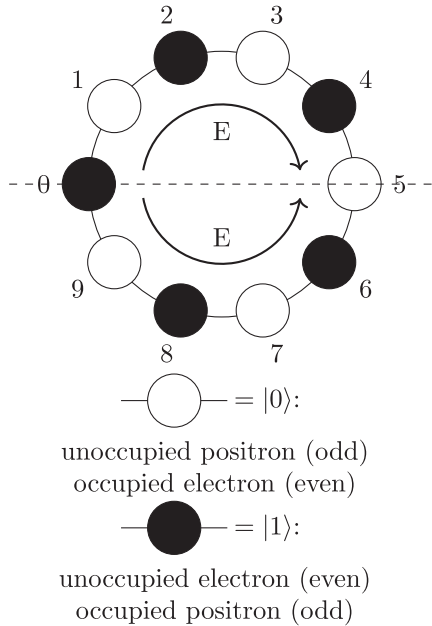

FIG. 1. The ground state of the free Hamiltonian, $|10101\rangle$. The dotted line connects the site 0 and the site 5. It implies the parity symmetry maps n site to $(10 - n)$ site and makes the upper and lower part of the figure equivalent.

our simulation. An excited electron changes $|1\rangle$ to $|0\rangle$ on the 0th, 2nd, or 4th qubit, while an excited positron changes $|0\rangle$ to $|1\rangle$ on the 1st or 3rd qubit. Since charge is conserved, there exists a physical subspace in which the states contain three 1's and two 0's given the charge-zero initial state. Such principle turns out to be the key to solve the eigenstates of the system and to reduce hardware noises.

After having the initial state $|10101\rangle$, we will turn on the nearest-neighbor lattice-site interactions $H_{0,k}$. One approach is to adiabatically turn on the kinetic term $H_{0,k}$ [3], but this is a resource-consuming procedure since we need gradually turn on the kinetic term, requiring circuit depth exceeding the limits of hardware available in the NISQ era. Instead, we use the variational quantum eigensolver (VQE) [59] method to find the ground state of the Hamiltonian H_0 with a much shallower circuit. The ansatz of the VQE circuit mimics the Hamiltonian of the system and contains nine parametrized gates which are rotational operators along the y and z axis of the Bloch sphere. The 9 parameters are optimized via minimizing the expectation value of the free Hamiltonian H_0 to obtain the vacuum state $|\Omega_{\text{VQE}}\rangle$. The vacuum state is compared to the exact numerical solutions of the vacuum states of H_0, $|\Omega_{\text{exact}}\rangle$. As a result of the VQE method, the fidelity $|\langle\Omega_{\text{VQE}}|\Omega_{\text{exact}}\rangle|^2$ to be larger than 99%. Hence the VQE method finds a correct vacuum with great accuracy but a few quantum gates. Note that in the VQE method the operators in the circuit are all charge conserved, such that the states will stay in the physical subspace.

B. Time evolution

We start with the VQE vacuum state $|\Omega_{\text{VQE}}\rangle$ at the beginning of the simulation, $t = 0$. The state is evolved with the full Hamiltonian $H = H_0 + H_I$. The parity even (odd) Hamiltonian H_+ (H_-) is a function of Pauli spin operators with the Jordan-Wigner transformation [58], and is further decomposed into three parts for constructing the quantum algorithm,

$$H_{+1} = \sum_{n=0}^{4}[(-1)^n m + eEan]\frac{\sigma_3(n)}{2}, \quad (8)$$

$$H_{+2} = \frac{1}{\sqrt{2}a}[\sigma^+(0)\sigma^-(1) + \sigma^+(1)\sigma^-(0)]$$
$$+ \frac{1}{2a}[\sigma^+(2)\sigma^-(3) + \sigma^+(3)\sigma^-(2)] \quad (9)$$

$$H_{+3} = \frac{1}{2a}\sum_{n=1,3}[\sigma^+(n)\sigma^-(n+1) + \sigma^+(n+1)\sigma^-(n)], \quad (10)$$

with $\sigma^\pm(n) = [\sigma_1(n) \pm i\sigma_2(n)]/2$. See Eqs. (A23) to (A31) in Appendix A for more details. The unitary time evolution $U(t)$ can be expanded by using Suzuki-Trotter formulas with n_t steps [60,61],

$$U(t) = e^{-iH_+ t} = \left(\prod_{j=1}^{3} e^{-iH_{+j}\delta t} \right)^{n_t} + \mathcal{O}(t^2/n_t), \quad (11)$$

where $\delta t = t/n_t$. The Hamiltonian decomposition in Eqs. (8) to (10) is optimized by the quantum gate implementation. For each time step, $\exp(-iH_{+1}\delta t)$ is implemented by the rotation gate along the z-axis, R_z, while $\exp(-iH_{+2}\delta t)$ and $\exp(-iH_{+3}\delta t)$ are realized by two CNOT and one controlled x-axis rotation gate R_x. In the simulation, the number of time steps is determined by trading off between Trotterization errors and hardware quantum noises.

C. Measurement

After n_t steps of evolution, we should turn off the kinetic term adiabatically then measure the probability of being the vacuum state. Such adiabatic turn-off is equivalent to applying an inverse VQE operator that we employed previously to make $|\Omega_{VQE}\rangle$. The vacuum persistence probability is measured by the frequency of the state $|10101\rangle$:

$$P_{\text{vac,raw}} = \frac{n_{\text{vac}}}{n_{\text{shot}}}, \quad (12)$$

where n_{shot} is the total number of measurements, n_{vac} is the number of the vacuum state $|10101\rangle$ within the measurement outcomes.

Although all of the previous procedures in our algorithm are charge conserved, the quantum noises can give nonzero charge final states. We propose to consider the physical states and remove the nonzero charge states because it will reduce the hardware errors. We obtain the number of created electrons and positrons by counting the number of $|0\rangle$ on the 0th, 2nd, and 4th qubits and the number of $|1\rangle$ on the 1st and 3rd qubits. It is because a charged-zero state always has equal numbers of electrons and positrons. In other words, there are always three $|1\rangle$ and two $|0\rangle$ out of the five qubits. Now we have

$$P_{\text{vac,corrected}} = \frac{n_{\text{vac}}}{n_{Q=0}}, \quad (13)$$

where $n_{Q=0}$ is the total number of final states $|\phi\rangle$ satisfying $\langle\phi|Q_+|\phi\rangle$ within the measurement outcomes. Q_+ is the charge operator defined by Eq. (A33) in Appendix A. From the definition of Q_+ we see that a charge-zero state has exactly three $|1\rangle$ and two $|0\rangle$ out of the five qubits. Using this approach in the measurement, we remove charge-nonzero states from the subspace. Suppose that the probability of a single bit flip error is of $O(\epsilon)$, then it needs at least two bit flips to return to the physical subspace. Therefore, when we measure the vacuum persistence probability by the frequency of $|10101\rangle$ restricted in the physical subspace, the hardware error is suppressed from $O(\epsilon)$ to $O(\epsilon^2)$.

IV. SCHWINGER PAIR PRODUCTION RESULTS

In this section, we analyze the numerical results of the Schwinger pair production with IBM quantum computers. Our analysis is based on the simulations running on an IBM machine, *ibm_lagos*, and on the simulations given by simulators from QISKIT [62] by turning off the quantum noises. The quantum simulation results are compared to the theoretical predication, and they are consistent within the experimental uncertainties. On the IBM quantum computer, following the dimension reduction method in the previous sections, we simulate the $(1+1)$D Schwinger effect with different effective masses $m' = \sqrt{m^2 + p_\perp^2}$ in parallel. By repeating the experiments and measuring the final states a large number of times, we deduce the vacuum persistent probability $P_{\text{vac}}(t)$ and the $(1+1)$D vacuum decay rate Γ_{1+1}. The decay rate in $(3+1)$D is obtained by integrating the decay rate Γ_{1+1} over the transverse momentum as Eq. (5). In the end, we discuss the uncertainties from the quantum simulation.

A benchmark point is chosen to demonstrate the validity of the quantum algorithm, where the parameters are given as

$$eE = 20, \qquad a = 0.45, \quad (14)$$

the number of lattice sites (qubits) $N = 5$ and the time step $n_t = 3$ for the Suzuki-Trotter expansion. Here we set $m = 1$ as a unit, the spacing a is determined by restricting the error within 10%, and $eE = 20$ represents a strong electric field. A weaker electric field takes a longer time in simulations to observe the vacuum decay, while a much stronger electric field will quickly populate quite a few electrons and positrons, such that the correction to the decay rate is not negligible both in theory and experiments. Hence we choose this intermediate value of eE.

The probability of the final states being the vacuum state $|10101\rangle$ denoted as the vacuum persistence probability $P_{\text{vac}}(t)$, is measured at different times. As an example, the probability for $m' = 1.4$ is shown in Fig. 2, and $P_{\text{vac}}(t)$ for other masses is presented in the Appendix. In Fig. 2, the numerical solution of the Hamiltonian in Eqs. (8) to (10) is shown in the dotted line. The numerical calculation gives the expected results for simulations to compare to. Also, it tells whether the parameters, a, eE, and N is a proper choice by comparing to the Schwinger pair production rate derived from the continuous spacetime, which is given as [63]

$$\Gamma_{1+1}(m) = \frac{eE}{2\pi} \log(1 - e^{-\frac{\pi m^2}{eE}}). \quad (15)$$

We perform the simulation in two systems: IBM's quantum simulators and quantum computers. The IBM simulators are designed to simulate and test the quantum computers, where we turn off quantum noises in the simulators to validate our quantum algorithm in an ideal situation. As shown in Fig. 2, the noiseless simulation results are aligned with the "exact numerical calculation." The quantum simulation results
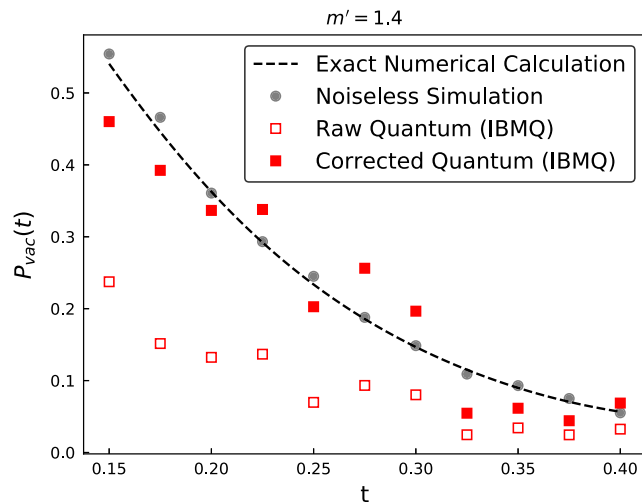
FIG. 2. Vacuum persistent probability for the effective mass $m' = 1.4$, $eE = 20$, $a = 0.45$, the number of lattice sites (qubits) $N = 5$ and the time step $n_t = 3$ for the Suzuki-Trotter expansion. The dashed curve corresponds to the exact numerical solution of the Hamiltonian. The simulation results on a noiseless simulator are shown in the gray dots. The *ibm_lagos* quantum computer results given by Eq. (12) are shown in the hallow square. The solid squares given by Eq. (13) are the corrected results to the quantum simulation by restricting to the charger-conserving subspace.

FIG. 3. Vacuum decay rates versus effective masses m'. The solid curve corresponds to the theoretical predications from QED in continuous space-time given by Eq. (15). The fitting results of the noiseless simulator are shown in the gray dots. The results from the IBM *ibm_lagos* are shown in the square data points.

shown in the red hollow squares deviate from the exact solution due to the large noises. After removing the states having nonzero charges to restrict the final states in the physical subspace, we obtain the corrected quantum simulation results close to the theoretical ones.

For a given effective mass m', the persistent vacuum probability $P_{vac}(t)$ data are fitted by an exponential function of $c_1 \exp(-\Gamma_{1+1}(m') \times \text{volume} \times t)$ with a normalization factor c_1 and volume $= aN$. The fitting results give the decay rate per volume $\Gamma_{1+1}(m')$ and are shown in Fig. 3. Note that we choose a time range to fit the exponential curve and the normalization c_1 is set as a free parameter. In the case of $m' = 1.4$, the time region is taken as $0.10 < t < 0.45$; for other masses, the range is given in the caption of Fig. 4 in the Appendix C. The time range is set by considering that there is a transient effect at the beginning of time due to suddenly turning on the electric field and back reactions for a large time due to finite spatial size.

Integrating the $\Gamma_{1+1}(m')$ over the transverse momentum as Eq. (5) gives the electron-positron pair production rate in $(3 + 1)$D. Here we only consider the electron-positron pair production with the transverse momentum $p_{\perp}^2 \leq 3$, i.e., $m' \leq 2$, due to larger quantum noises for larger m'. The decay rate from the theoretical predication of QED is 0.58, the noiseless simulator result is 0.56, and the corrected quantum computer gives the decay rate 0.60.

There are various uncertainties in the quantum simulation, originated from space and time discretization, statistical error, and hardware noises, in which the hardware
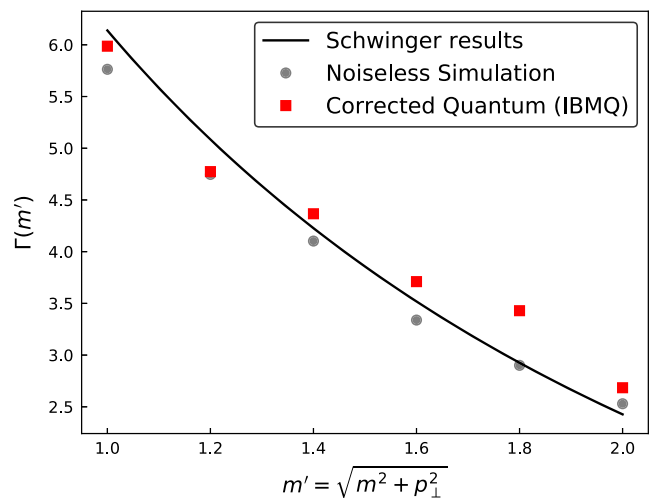
noises are the dominant ones. First, modeling the Schwinger effect in a lattice as Eqs. (8) to (10) introduces discretization error and truncation error by choosing the spacing a and the finite size $L = Na$. The errors from spacing and finite size are of orders $\mathcal{O}(a)$ and $\mathcal{O}(1/L^2)$, respectively. Here taking $N = 5$, $a = 0.45$ in the benchmark model gives the numerical solution of the Hamiltonian close to the theoretical predication of QED, which can be seen from comparing the Schwinger results to the noiseless simulation results in Fig. 3. Second, we experience statistical error of order $\mathcal{O}(1/\sqrt{n_{shot}})$ either on a simulator or a quantum computer with n_{shot} measurement shots. We take $n_{shot} = 8192$ to make sure the statistical error is subdominant compared to the other ones. Third, n_t Trotter steps in time introduces an error of order $\mathcal{O}(t^2/n_t)$. Here we choose $n_t = 3$ to give accurate enough simulation results and moderate circuit depth. Finally, hardware noises, especially readout errors and CNOT gate errors, in the NISQ era are quite large. On the *ibm_lagos* quantum computer the readout errors and CNOT gate errors are both about 1%. The VQE transformation as well as each Trotter step takes 8 CNOT gates, such that the whole circuit contains 40 CNOT gates. Hardware noises are relieved by restricting to the charge-conserved subspace. We could also apply readout error mitigation [64] or CNOT gate noise mitigation [65] to further reduce hardware noise, which we would like to explore in future works.

V. CONCLUSION

In this article, we demonstrate a quantum algorithm to simulate the nonperturbative phenomenon of the Schwinger effect in $(3 + 1)$D by using IBM's digital quantum

computers. The number of qubits, the depth of the circuit are reduced suitable to the NISQ area, and the quantum noise is under control to get the Schwinger pair production rate. We manage to perform the quantum simulation in 5-qubit, by treating the gauge field A^μ as a background field, finding the Hamiltonian diagonalization and further reducing the resources by parity symmetry. In the real-time quantum simulation, we prepare the ground state, evolve it to a given time with a few time-step and measure the final states. The depth of the circuit is shortened by implementing the VQE algorithm instead of adiabatic turn on(off). In the measurement, the hardware noises are relieved by restricting to the charge-conserving final states. We implement the algorithm on IBM's quantum computers also in the noiseless simulators. By analyzing the results and comparing them to the exact numerical calculation and theoretical predication of the Schwinger effect, we conclude that the results are consistent within uncertainties. This methodology can apply to some quantum field theory questions related to effective actions. We look forward to future studies of quantum simulation of QFT beyond one spatial dimension.

ACKNOWLEDGMENTS

APPENDIX A: THEORETICAL SETUP

1. Continuum formulation, $(3+1)$D to $(1+1)$D

In this section we show that the Schwinger pair-production in an electric background field in $(3 + 1)$D can be decomposed into a $(1 + 1)$D QED problem (i.e., the Schwinger model [66,67]).

First, we define the $(3 + 1)$D Dirac field in the Schrödinger picture

$$\psi(\vec{x}) = \int \frac{d^3 p}{(2\pi)^3} \frac{1}{\sqrt{2\omega_p}} e^{i\vec{p}\cdot\vec{x}} \sum_s (a_{\vec{p}}^s u^s(\vec{p}) + b_{-\vec{p}}^s v^s(-\vec{p}))$$

$$= \int \frac{dp_x dp_y}{(2\pi)^2} e^{i(p_x x + p_y y)} \sum_s \psi_s(z, p_x, p_y), \qquad (A1)$$

where

$$\psi_s(z, p_x, p_y) = \int \frac{dp_z}{2\pi} \frac{1}{\sqrt{2\omega_p}} e^{ip_z z} (a_{\vec{p}}^s u^s(\vec{p}) + b_{-\vec{p}}^s v^s(-\vec{p})). \qquad (A2)$$

The free Hamiltonian is of the form

$$H = \int d^3 x \psi^\dagger (-i\gamma^0 \vec{\gamma} \cdot \nabla + m\gamma^0)\psi$$

$$= \int dz \int \frac{dp_x dp_y}{(2\pi)^2} \sum_s \psi_s^\dagger h \psi_s, \qquad (A3)$$

where gamma matrices are in the Dirac basis

$$\gamma^0 = \begin{pmatrix} I_{2\times 2} & 0 \\ 0 & -I_{2\times 2} \end{pmatrix}, \qquad \gamma^i = \begin{pmatrix} 0 & \sigma^i \\ -\sigma^i & 0 \end{pmatrix}, \qquad (A4)$$

and

$$h = \begin{pmatrix} m & 0 & -i\partial_z & p_x - ip_y \\ 0 & m & p_x + ip_y & i\partial_z \\ -i\partial_z & p_x - ip_y & -m & 0 \\ p_x + ip_y & i\partial_z & 0 & -m \end{pmatrix}. \qquad (A5)$$

By doing the unitary transformation

$$U = \frac{1}{\sqrt{2m'}} \begin{pmatrix} \sqrt{m' + m} & -\frac{p_x\sigma_x + p_y\sigma_y}{\sqrt{m'+m}} \\ \frac{p_x\sigma_x + p_y\sigma_y}{\sqrt{m'+m}} & \sqrt{m' + m} \end{pmatrix}, \qquad (A6)$$

we obtain

$$h' = U^\dagger h U = \begin{pmatrix} m' I_{2\times 2} & -i\partial_z\sigma_z \\ -i\partial_z\sigma_z & -m' I_{2\times 2} \end{pmatrix}, \qquad (A7)$$

where $m' = \sqrt{m^2 + p_x^2 + p_y^2}$ and we define $\tilde{\psi}_s = U^\dagger \psi_s$.

One can easily find the eigenvectors of h', which are also the solutions to the free-particle Dirac equation, to be

$$u'_{\frac{1}{2}}(\vec{p}) \propto \begin{pmatrix} m' + \omega_p \\ 0 \\ p_z \\ 0 \end{pmatrix}, \qquad v'_{\frac{1}{2}}(\vec{p}) \propto \begin{pmatrix} m' + \omega_p \\ 0 \\ -p_z \\ 0 \end{pmatrix},$$

$$u'_{-\frac{1}{2}}(\vec{p}) \propto \begin{pmatrix} 0 \\ m' + \omega_p \\ 0 \\ -p_z \end{pmatrix}, \qquad v'_{-\frac{1}{2}}(\vec{p}) \propto \begin{pmatrix} 0 \\ m' + \omega_p \\ 0 \\ p_z \end{pmatrix},$$

$$(A8)$$

which means the 2,4 components of $\tilde{\psi}_{1/2}$ and the 1,3 components of $\tilde{\psi}_{-1/2}$ are always zero. Thus it is natural to define the following two-component spin states

$$\tilde{\psi}_{1/2}^{(2)} = \begin{pmatrix} \tilde{\psi}_1 \\ \tilde{\psi}_3 \end{pmatrix}, \qquad \tilde{\psi}_{-1/2}^{(2)} = \begin{pmatrix} \tilde{\psi}_2 \\ \tilde{\psi}_4 \end{pmatrix}. \qquad (A9)$$

Now the Hamiltonian can be written as

$$H = \sum_s \int \frac{dp_x dp_y}{(2\pi)^2} \tilde{H}_s^{(2)}, \qquad (A10)$$

where

$$\tilde{H}_s^{(2)} = \int dz \tilde{\psi}_s^{(2)\dagger}(\pm i\partial_z \tilde{\gamma}^0 \tilde{\gamma}^1 + m' \tilde{\gamma}^0)\tilde{\psi}_s^{(2)} \qquad (A11)$$

has exactly the same form of the Hamiltonian in $(1+1)$D, and

$$\tilde{\gamma}^0 = \begin{pmatrix} 1 & 0 \\ 0 & -1 \end{pmatrix}, \qquad \tilde{\gamma}^1 = \begin{pmatrix} 0 & -1 \\ 1 & 0 \end{pmatrix} \qquad (A12)$$

are the gamma matrices in 2D; the sign ambiguity in Eq. (A11) can be absorbed by redefining $\tilde{\gamma}^1$.

Given a static electric background field along the z axis, choosing the axial gauge $\vec{A} = 0, A_0 = A_0(z)$, we need to add the following interaction term into the Hamiltonian:

$$H_I = \int d^3x e A_0 \psi^\dagger \psi. \qquad (A13)$$

Following the same procedure, the interaction term can be written as

$$H_I = \sum_s \int \frac{dp_x dp_y}{(2\pi)^2} \tilde{H}_{I,s}^{(2)}, \qquad (A14)$$

where

$$\tilde{H}_{I,s}^{(2)} = \int dz e A_0 \tilde{\psi}_s^{(2)\dagger} \tilde{\psi}_s^{(2)} \qquad (A15)$$

again exactly matches with the interaction term in 2D.

The charge operator, which can be directly read from Eqs. (A13) and (A15), has the following form:

$$Q^{(4)} = \int d^3x \psi^\dagger \psi = \sum_s \int \frac{dp_x dp_y}{(2\pi)^2} Q_s^{(2)}, \qquad (A16)$$

where

$$Q_s^{(2)} = \int dz \tilde{\psi}_s^{(2)\dagger} \tilde{\psi}_s^{(2)} \qquad (A17)$$

is the charge operator in the 2D form.

Now the $(3+1)$D QED problems are reduced to $(1+1)$D QED with the mass m replaced by $m' = \sqrt{m^2 + p_x^2 + p_y^2}$, scanning over the momentum space along the x and y direction and summing over spin.

It can be shown that the vacuum decay rates of the Schwinger effect in $(3+1)$D are related to the rate in $(1+1)$D [63]

$$\Gamma_{3+1}(m) = 2 \int \frac{dp_x dp_y}{(2\pi)^2} \Gamma_{1+1}(m'). \qquad (A18)$$

2. Lattice formulation of $(1+1)$D fermions

Having shown that the Schwinger pair production of fermions with mass m and momentum $\vec{p}$ in $(3+1)$D is equivalent with the pair production of $(1+1)$D fermions

with mass $m' = \sqrt{m^2 + p_x^2 + p_y^2}$ and momentum $p = p_z$, in this section we present the discretization of the $(1+1)$D Hamiltonian Eqs. (A11) and (A15) on a lattice grid periodic boundary condition. We place the fermion field on a 1D lattice with spacing a, labeled by n. To avoid the fermion doubling problem, we adopt the staggered fermion approach [55,56], where the upper(lower) component of $\tilde{\psi}_s$ is mapped to the fermion field $\phi(n)$ at even (odd) lattice sites

$$\phi(n)/\sqrt{a} \rightarrow \begin{cases} \tilde{\psi}_{\text{upper}}^{(2)}(na) & n \text{ even,} \\ \tilde{\psi}_{\text{lower}}^{(2)}(na) & n \text{ odd.} \end{cases} \qquad (A19)$$

Fermion fields on each site satisfy the following anticommutation relation

$$\{\phi^\dagger(m), \phi(n)\} = \delta_{mn}, \quad \{\phi(m), \phi(n)\} = 0, \quad n \in [0, N-1]. \qquad (A20)$$

The fermion fields have the boundary condition of $\phi(0) = \phi(N)$.

The Hamiltonian Eqs. (A11) and (A15) are then discretized to be

$$H_0 = \frac{i}{2a} \sum_n [\phi^\dagger(n)\phi(n+1) - \phi^\dagger(n+1)\phi(n)]$$
$$+ m \sum_n (-1)^n \phi^\dagger(n)\phi(n), \qquad (A21)$$

$$H_I = \sum_n e A_0(na)\phi^\dagger(n)\phi(n). \qquad (A22)$$

We adopt $A_0(z) = -E|z|$ with origin mapped at the site $N/2$. Observing that the Hamiltonian $H = H_0 + H_I$ is invariant under the parity transformation $P: \tilde{\psi}_s^{(2)}(z) \rightarrow \tilde{\gamma}^0 \tilde{\psi}_s^{(2)}(-z)$ for continuum or $P: \phi(m) \rightarrow (-1)^m \phi(N-m)$ for discrete, we could define the parity even and odd field

$$\phi_\pm(m) = \frac{\phi(m) \pm (-1)^m \phi(N-m)}{\sqrt{2}},$$
$$m = 1, 2, ..., \frac{N}{2} - 1, \qquad (A23)$$

$$\phi_+(0) = \phi(0), \qquad \phi_-(0) = 0,$$
$$\phi_\pm\left(\frac{N}{2}\right) = \frac{1 \pm (-1)^{N/2}}{2} \phi\left(\frac{N}{2}\right). \qquad (A24)$$

which satisfy the anticommutation relations

$$\{\phi_\pm^\dagger(m), \phi_\pm(n)\} = \delta_\pm \delta_{mn}. \qquad (A25)$$

The Hamiltonian is further divided into two parts $H = H_+ + H_-$, which can be simulated separately

$$H_+ = \frac{i}{2a} \sum_{m=1}^{N/2-2} [\phi^\dagger(m)\phi(m+1) - \phi^\dagger(m+1)\phi(m)]$$

$$+ \frac{i}{\sqrt{2}a} [\phi^\dagger(0)\phi(1) - \phi^\dagger(1)\phi(0)]$$

$$+ \sum_{m=0}^{N/2-1} [(-1)^m M + eEam]\phi^\dagger(m)\phi(m), \quad (A26)$$

$$H_- = \frac{i}{2a} \sum_{m=1}^{N/2-2} [\phi^\dagger(m)\phi(m+1) - \phi^\dagger(m+1)\phi(m)]$$

$$+ \frac{i}{\sqrt{2}a} \left[\phi^\dagger\left(\frac{N}{2}-1\right)\phi\left(\frac{N}{2}\right) - \phi^\dagger\left(\frac{N}{2}\right)\phi\left(\frac{N}{2}-1\right) \right]$$

$$+ \sum_{m=1}^{N/2} [(-1)^m M + eEam]\phi^\dagger(m)\phi(m). \quad (A27)$$

The fermion field operators can be written in terms of spin operators by applying the Jordan-Winger transformation [58]

$$\phi(n) = \prod_{l<n} [i\sigma_3(l)]\sigma^-(n), \quad (A28)$$

$$\phi^\dagger(n) = \prod_{l<n} [-i\sigma_3(l)]\sigma^+(n), \quad (A29)$$

where $\sigma^\pm(n) = [\sigma_1(n) \pm i\sigma_2(n)]/2$.

The Hamiltonian is then converted to

$$H_+ = \frac{1}{2a} \sum_{n=1}^{N/2-2} [\sigma^+(n)\sigma^-(n+1) + \sigma^+(n+1)\sigma^-(n)]$$

$$+ \frac{1}{\sqrt{2}a} [\sigma^+(0)\sigma^-(1) + \sigma^+(1)\sigma^-(0)]$$

$$+ \sum_{n=0}^{N/2-1} [(-1)^n m + eEan]\frac{\sigma_3(n)+1}{2}, \quad (A30)$$

$$H_- = \frac{1}{2a} \sum_{n=1}^{N/2-2} [\sigma^+(n)\sigma^-(n+1) + \sigma^+(n+1)\sigma^-(n)]$$

$$+ \frac{1}{\sqrt{2}a} \left[\sigma^+\left(\frac{N}{2}-1\right)\sigma^-\left(\frac{N}{2}\right) + \sigma^+\left(\frac{N}{2}\right)\sigma^-\left(\frac{N}{2}-1\right) \right]$$

$$+ \sum_{n=1}^{N/2} [(-1)^n m + eEan]\frac{\sigma_3(n)+1}{2}, \quad (A31)$$

which is ready to be simulated on a digital quantum computer.

The charge operators, which again can be read from Eq. (A22) and Eqs. (A30)–(A31), are given by

$$Q = \sum_n \phi^\dagger(n)\phi(n) \quad (A32)$$

for the staggered fermion fields, and

$$Q_+ = \left(\sum_{n=0}^{N/2-1} \frac{\sigma_3(n)}{2} \right) + \frac{1}{2}, \quad (A33)$$

$$Q_- = \left(\sum_{n=1}^{N/2} \frac{\sigma_3(n)}{2} \right) - \frac{1}{2} \quad (A34)$$

for the spin operators with even and odd parity, where the $\pm\frac{1}{2}$ are chosen for convenience to make sure that

$$\langle 10101|Q_+|10101\rangle = \langle 01010|Q_-|01010\rangle = 0 \quad (A35)$$

for $N = 10$.

APPENDIX B: DEMONSTRATION OF QUANTUM CIRCUITS

We decompose the parity even Hamiltonian into 3 pieces $H_+ = H_{+1} + H_{+2} + H_{+3}$:
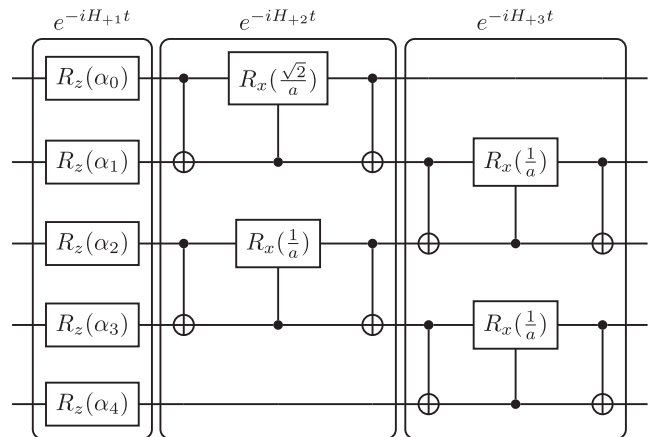
$$H_{+1} = \sum_{n=0}^{N/2-1} [(-1)^n m + eEan]\frac{\sigma_3(n)}{2}, \quad (B1)$$

$$H_{+2} = \frac{1}{\sqrt{2}a} [\sigma^+(0)\sigma^-(1) + \sigma^+(1)\sigma^-(0)]$$

$$+ \frac{1}{2a} \sum_{n=2}^{N/2-3} [\sigma^+(n)\sigma^-(n+1) + \sigma^+(n+1)\sigma^-(n)],$$

$$(B2)$$

$$H_{+3} = \frac{1}{2a} \sum_{n=1}^{N/2-2} [\sigma^+(n)\sigma^-(n+1) + \sigma^+(n+1)\sigma^-(n)],$$

$$(B3)$$

on which we could apply Suzuki-Trotter formula and simulate the time evolution.

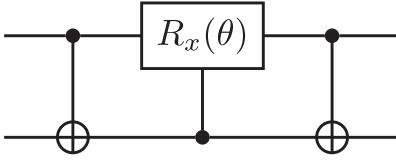The quantum circuit for each Trotter step is shown below ($N/2 = 5$)


where $\alpha_k = (-1)^k m + eEak$. Single qubit gates

$$R_P(\theta) = e^{-i\frac{\sigma_P}{2}\theta}, \quad \text{where } P = x, y, z, \tag{B4}$$

represent rotations along the axis P of the Bloch sphere.

The exponential of the operator $\sigma^+(n)\sigma^-(n+1) + \sigma^+(n+1)\sigma^-(n)$ in the kinetic term can be implemented by the following gates:

$$e^{-i\frac{\theta}{2}[\sigma^+(n)\sigma^-(n+1)+\sigma^+(n+1)\sigma^-(n)]} =$$

where a controlled-x rotation is sandwiched by two CNOT gates, and is further transpiled into basic gates of *ibm_lagos* in the following structure with two CNOT gates
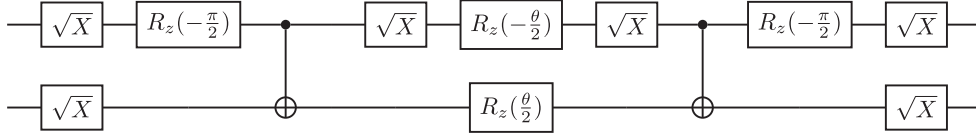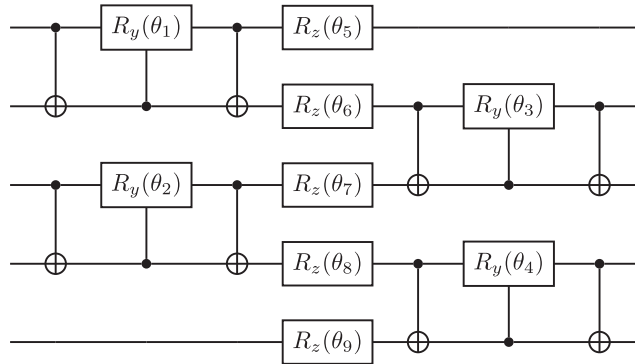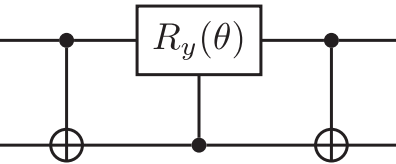

Note that

$$[Q_+, \sigma_3(n)] = [Q_+, \sigma^+(n)\sigma^-(n+1) + \sigma^+(n+1)\sigma^-(n)] = 0, \tag{B5}$$

which means the Hamiltonian H_+ commutes with the charge operator Q_+, thus the time evolution process is charge preserving.

The VQE ansatz we used to generate the ground state for H_0 is the following circuit with 9 parameters:

where we use controlled-y rotations sandwiched by two CNOT gates to generate entanglements between adjacent qubits, which can be represented by the exponential of the operator $i\sigma^+(n)\sigma^-(n+1) - i\sigma^+(n+1)\sigma^-(n)$,

$$e^{-\frac{\theta}{2}[\sigma^+(n)\sigma^-(n+1)-\sigma^+(n+1)\sigma^-(n)]} =$$

We then insert five z rotations in the middle to generate phases.

Note that

$$[Q_+, \sigma^+(n)\sigma^-(n+1) - \sigma^+(n+1)\sigma^-(n)] = [Q_+, \sigma_3(n)] = 0, \tag{B6}$$

The VQE operator is also charge preserving.

APPENDIX C: PLOTS OF VACUUM PERSISTENCE PROBABILITY FOR DIFFERENT MASSES
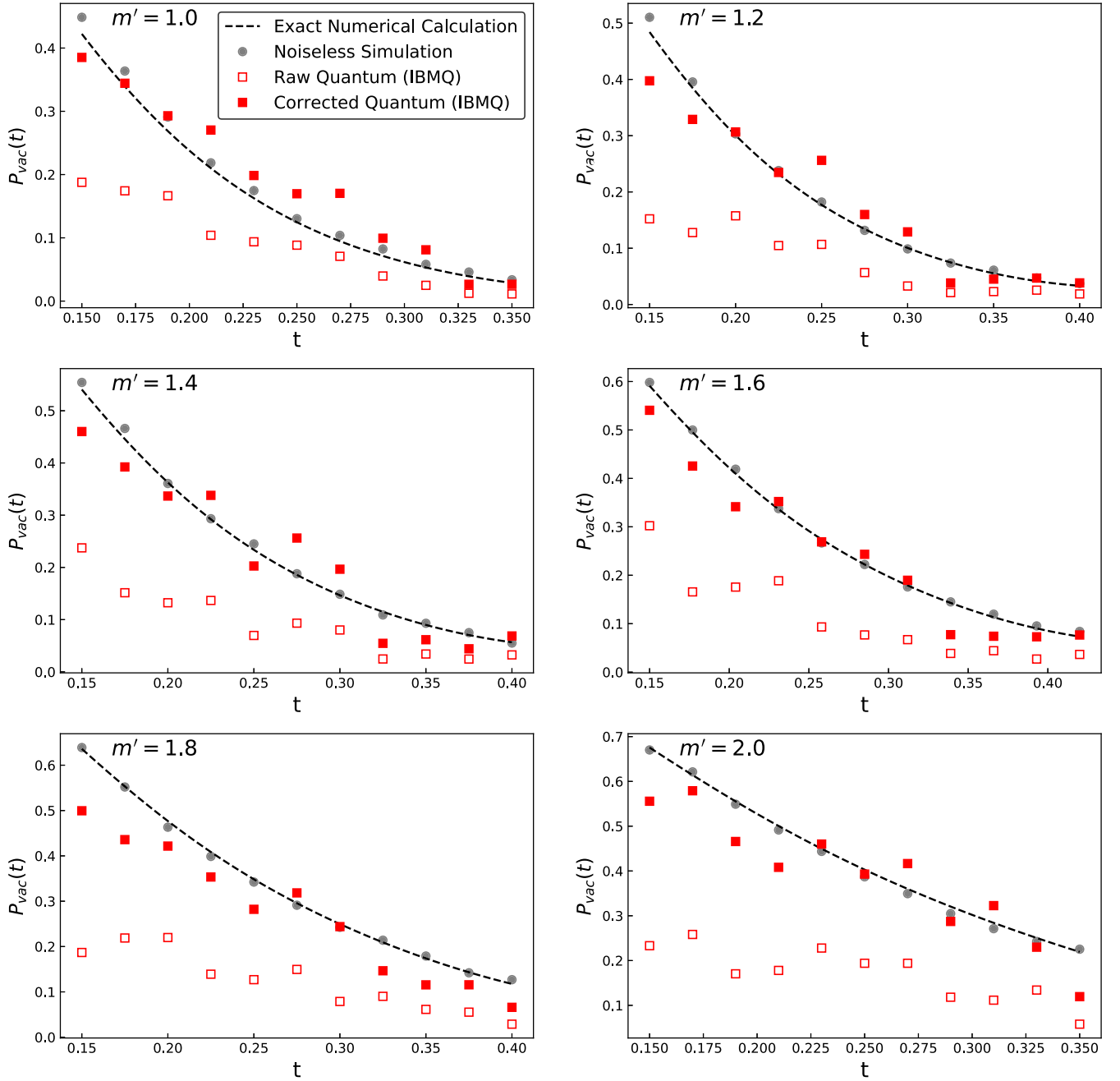

FIG. 4.   Vacuum persistent probability for the effective masses $m' = 1.0, 1.2, 1.4, 1.6, 1.8,$ and 2.0, $eE = 20$, $a = 0.45$, the number of lattice sites (qubits) $N = 5$ and the time step $n_t = 3$ for the Suzuki-Trotter expansion. The dashed curve corresponds to the exact numerical solution of the Hamiltonian. The gray dots show the simulation results on a noiseless simulator. The hollow squares show results from the *ibm_lagos* quantum computer given by Eq. (12). The solid squares given by Eq. (13) are the corrected results to the quantum simulation by restricting to physical subspace. The time regions we choose are $0.15 < t < 0.35$ for $m = 1.0$ and 2.0, $0.15 < t < 0.40$ for $m = 1.2, 1, 4,$ and 1.8, $0.15 < t < 0.42$ for $m = 1.6$.

[1] S. P. Jordan, K. S. M. Lee, and J. Preskill, Quantum algorithms for quantum field theories, Science **336,** 1130 (2012).

[2] S. P. Jordan, K. S. M. Lee, and J. Preskill, Quantum computation of scattering in scalar quantum field theories, Quantum Inf. Comput. **14,** 1014 (2014),

[3] S. P. Jordan, K. S. M. Lee, and J. Preskill, Quantum algorithms for fermionic quantum field theories, arXiv:1404.7115.

[4] S. P. Jordan, H. Krovi, K. S. M. Lee, and J. Preskill, BQP-completeness of scattering in scalar quantum field theory, Quantum **2,** 44 (2018).

[5] J. Preskill, Simulating quantum field theory with a quantum computer, Proc. Sci., LATTICE2018 (**2018**) 024 [arXiv:1811.10085].

[6] L. Kofman, A. D. Linde, and A. A. Starobinsky, Reheating After Inflation, Phys. Rev. Lett. **73,** 3195 (1994).

[7] L. Kofman, A. D. Linde, and A. A. Starobinsky, Towards the theory of reheating after inflation, Phys. Rev. D **56,** 3258 (1997).

[8] P. B. Greene, L. Kofman, A. D. Linde, and A. A. Starobinsky, Structure of resonance in preheating after inflation, Phys. Rev. D **56,** 6175 (1997).

[9] Y.-Z. Qian, G. M. Fuller, G. J. Mathews, R. Mayle, J. R. Wilson, and S. E. Woosley, A Connection Between Flavor Mixing of Cosmologically Significant Neutrinos and Heavy Element Nucleosynthesis in Supernovae, Phys. Rev. Lett. **71,** 1965 (1993).

[10] Y. Z. Qian and G. M. Fuller, Neutrino-neutrino scattering and matter enhanced neutrino flavor transformation in Supernovae, Phys. Rev. D **51,** 1479 (1995).

[11] G. L. Fogli, E. Lisi, A. Marrone, and A. Mirizzi, Collective neutrino flavor transitions in supernovae and the role of trajectory averaging, J. Cosmol. Astropart. Phys. 12 (2007) 010.

[12] M. Troyer and U.-J. Wiese, Computational Complexity and Fundamental Limitations to Fermionic Quantum Monte Carlo Simulations, Phys. Rev. Lett. **94,** 170201 (2005).

[13] A. Alexandru, G. Basar, P. F. Bedaque, S. Vartak, and N. C. Warrington, Monte Carlo Study of Real Time Dynamics on the Lattice, Phys. Rev. Lett. **117,** 081602 (2016).

[14] J. S. Schwinger, On gauge invariance and vacuum polarization, Phys. Rev. **82,** 664 (1951).

[15] A. Casher, H. Neuberger, and S. Nussinov, Chromoelectric flux tube model of particle production, Phys. Rev. D **20,** 179 (1979).

[16] H. Neuberger, Finite time corrections to the chromoelectric flux tube model, Phys. Rev. D **20,** 2936 (1979).

[17] C. B. Chiu and S. Nussinov, A diagrammatic approach to pair production in slowly varying and constant fields, Phys. Rev. D **20,** 945 (1979).

[18] N. K. Glendenning and T. Matsui, Creation of anti-q q pair in a chromoelectric flux tube, Phys. Rev. D **28,** 2890 (1983).

[19] H. G. Dosch and D. Gromes, Theoretical foundation for treating decays allowed by the Okubo-Zweig-Iizuka rule and related phenomena, Phys. Rev. D **33,** 1378 (1986).

[20] S. W. Hawking, Particle creation by black holes, Commun. Math. Phys. **43,** 199 (1975); Erratum, Commun. Math. Phys. **46,** 206 (1976).

[21] T. Damour and R. Ruffini, Black hole evaporation in the Klein-Sauter-Heisenberg-Euler formalism, Phys. Rev. D **14,** 332 (1976).

[22] J. Preskill, Quantum Computing in the NISQ era and beyond, Quantum **2,** 79 (2018).

[23] T. Byrnes and Y. Yamamoto, Simulating lattice gauge theories on a quantum computer, Phys. Rev. A **73,** 022328 (2006).

[24] U.-J. Wiese, Ultracold quantum gases and lattice systems: Quantum simulation of lattice gauge theories, Ann. Phys. (Amsterdam) **525,** 777 (2013).

[25] U.-J. Wiese, Towards quantum simulating QCD, Nucl. Phys. **A931,** 246 (2014).

[26] A. Bermudez, G. Aarts, and M. Müller, Quantum Sensors for the Generating Functional of Interacting Quantum Field Theories, Phys. Rev. X **7,** 041012 (2017).

[27] L. García-Álvarez, J. Casanova, A. Mezzacapo, I. L. Egusquiza, L. Lamata, G. Romero, and E. Solano, Fermion-Fermion Scattering in Quantum Field Theory with Superconducting Circuits, Phys. Rev. Lett. **114,** 070502 (2015).

[28] E. Zohar, J. I. Cirac, and B. Reznik, Quantum simulations of lattice gauge theories using ultracold atoms in optical lattices, Rep. Prog. Phys. **79,** 014401 (2016).

[29] T. Pichler, M. Dalmonte, E. Rico, P. Zoller, and S. Montangero, Real-Time Dynamics in U(1) Lattice Gauge Theories with Tensor Networks, Phys. Rev. X **6,** 011023 (2016).

[30] A. Macridin, P. Spentzouris, J. Amundson, and R. Harnik, Electron-Phonon Systems on a Universal Quantum Computer, Phys. Rev. Lett. **121,** 110504 (2018).

[31] N. Klco and M. J. Savage, Digitization of scalar fields for quantum computing, Phys. Rev. A **99,** 052335 (2019).

[32] D. C. Hackett, K. Howe, C. Hughes, W. Jay, E. T. Neil, and J. N. Simone, Digitizing gauge fields: Lattice Monte Carlo results for future quantum computers, Phys. Rev. A **99,** 062341 (2019).

[33] M. Kreshchuk, W. M. Kirby, G. Goldstein, H. Beauchemin, and P. J. Love, Quantum simulation of quantum field theory in the light-front formulation, Phys. Rev. A **105,** 032418 (2022).

[34] J. F. Haase, L. Dellantonio, A. Celi, D. Paulson, A. Kan, K. Jansen, and C. A. Muschik, A resource efficient approach for quantum and classical simulations of gauge theories in particle physics, Quantum **5,** 393 (2021).

[35] T. F. Stetina, A. Ciavarella, X. Li, and N. Wiebe, Simulating effective QED on quantum computers, Quantum **6,** 622 (2022).

[36] Z. Davoudi, N. M. Linke, and G. Pagano, Toward simulating quantum field theories with controlled phonon-ion dynamics: A hybrid analog-digital approach, Phys. Rev. Res. **3,** 043072 (2021).

[37] S. Ramírez-Uribe, A. E. Rentería-Olivo, G. Rodrigo, G. F. R. Sborlini, and L. Vale Silva, Quantum algorithm for Feynman loop integrals, J. High Energy Phys. 05 (2022) 100.

[38] J. R. Stryker, Shearing approach to gauge invariant Trotterization, arXiv:2105.11548.

[39] N. Klco, A. Roggero, and M. J. Savage, Standard model physics and the digital quantum revolution:

Thoughts about the interface, Rep. Prog. Phys. **85**, 064301 (2022).

[40] A. Kan and Y. Nam, Lattice quantum chromodynamics and electrodynamics on a universal quantum computer, arXiv: 2107.12769.

[41] E. Zohar, J. I. Cirac, and B. Reznik, Cold-Atom Quantum Simulator for SU(2) Yang-Mills Lattice Gauge Theory, Phys. Rev. Lett. **110**, 125304 (2013).

[42] E. Zohar, J. I. Cirac, and B. Reznik, Simulating Compact Quantum Electrodynamics with Ultracold Atoms: Probing Confinement and Nonperturbative Effects, Phys. Rev. Lett. **109**, 125302 (2012).

[43] D. Banerjee, M. Dalmonte, M. Muller, E. Rico, P. Stebler, U. J. Wiese, and P. Zoller, Atomic Quantum Simulation of Dynamical Gauge Fields coupled to Fermionic Matter: From String Breaking to Evolution after a Quench, Phys. Rev. Lett. **109**, 175302 (2012).

[44] D. Banerjee, M. Bögli, M. Dalmonte, E. Rico, P. Stebler, U. J. Wiese, and P. Zoller, Atomic Quantum Simulation of U(N) and SU(N) Non-Abelian Lattice Gauge Theories, Phys. Rev. Lett. **110**, 125303 (2013).

[45] D. Marcos, P. Widmer, E. Rico, M. Hafezi, P. Rabl, U. J. Wiese, and P. Zoller, Two-dimensional lattice gauge theories with superconducting quantum circuits, Ann. Phys. (Amsterdam) **351**, 634 (2014).

[46] E. Zohar, A. Farace, B. Reznik, and J. I. Cirac, Digital lattice gauge theories, Phys. Rev. A **95**, 023604 (2017).

[47] E. A. Martinez *et al.*, Real-time dynamics of lattice gauge theories with a few-qubit quantum computer, Nature (London) **534**, 516 (2016).

[48] N. Klco, E. F. Dumitrescu, A. J. McCaskey, T. D. Morris, R. C. Pooser, M. Sanz, E. Solano, P. Lougovski, and M. J. Savage, Quantum-classical computation of Schwinger model dynamics using quantum computers, Phys. Rev. A **98**, 032331 (2018).

[49] C. W. Bauer, M. Freytsis, and B. Nachman, Simulating Collider Physics on Quantum Computers Using Effective Field Theories, Phys. Rev. Lett. **127**, 212001 (2021).

[50] A. M. Czajka, Z.-B. Kang, H. Ma, and F. Zhao, Quantum simulation of chiral phase transitions, J. High Energy Phys. 08 (2022) 209.

[51] K. Yeter-Aydeniz, E. F. Dumitrescu, A. J. McCaskey, R. S. Bennink, R. C. Pooser, and G. Siopsis, Scalar quantum field theories as a benchmark for near-term quantum computers, Phys. Rev. A **99**, 032306 (2019).

[52] M. Kreshchuk, S. Jia, W. M. Kirby, G. Goldstein, J. P. Vary, and P. J. Love, Light-front field theory on current quantum computers, Entropy **23**, 597 (2021).

[53] T. Li, X. Guo, W. K. Lai, X. Liu, E. Wang, H. Xing, D.-B. Zhang, and S.-L. Zhu, Partonic structure by quantum computing, Phys. Rev. D **105**, L111502 (2022).

[54] W. A. de Jong, K. Lee, J. Mulligan, M. Płoskoń, F. Ringer, and X. Yao, Quantum simulation of non-equilibrium dynamics and thermalization in the Schwinger model, Phys. Rev. D **106**, 054508 (2022).

[55] J. B. Kogut and L. Susskind, Hamiltonian formulation of Wilson's lattice gauge theories, Phys. Rev. D **11**, 395 (1975).

[56] T. Banks, L. Susskind, and J. B. Kogut, Strong coupling calculations of lattice gauge theories: $(1+1)$-dimensional exercises, Phys. Rev. D **13**, 1043 (1976).

[57] A. Casher, J. B. Kogut, and L. Susskind, Vacuum Polarization and the Quark Parton Puzzle, Phys. Rev. Lett. **31**, 792 (1973).

[58] P. Jordan and E. P. Wigner, über das paulische äquivalenzverbot, in *The Collected Works of Eugene Paul Wigner* (Springer, New York, 1993), pp. 109–129, 10.1007/978-3-662-02781-3_9.

[59] A. Peruzzo, J. McClean, P. Shadbolt, M.-H. Yung, X.-Q. Zhou, P. J. Love, A. Aspuru-Guzik, and J. L. O'brien, A variational eigenvalue solver on a photonic quantum processor, Nat. Commun. **5**, 4213 (2014).

[60] H. F. Trotter, On the product of semi-groups of operators, Proc. Am. Math. Soc. **10**, 545 (1959).

[61] M. Suzuki, Generalized Trotter's formula and systematic approximants of exponential operators and inner derivations with applications to many body problems, Commun. Math. Phys. **51**, 183 (1976).

[62] H. Abraham, I. Y. Akhalwaya, G. Aleksandrowicz, T. Alexander, G. Alexandrowics, E. Arbel, A. Asfaw, C. Azaustre, P. Barkoutsos, G. Barron *et al.*, QISKIT: An open-source framework for quantum computing, 2019, Zenodo, 10.5281/zenodo.2562111 (2019), 2562111.

[63] T. D. Cohen and D. A. McGady, The Schwinger mechanism revisited, Phys. Rev. D **78**, 036008 (2008).

[64] B. Nachman, M. Urbanek, W. A. de Jong, and C. W. Bauer, Unfolding quantum computer readout noise, npj Quantum Inf. **6**, 84 (2020).

[65] A. He, B. Nachman, W. A. de Jong, and C. W. Bauer, Resource efficient zero noise extrapolation with identity insertions, Phys. Rev. A **102**, 012426 (2020).

[66] J. S. Schwinger, Gauge invariance and mass. 2, Phys. Rev. **128**, 2425 (1962).

[67] J. H. Lowenstein and J. A. Swieca, Quantum electrodynamics in two-dimensions, Ann. Phys. (N.Y.) **68**, 172 (1971).